the cutoff frequency ω_c and the solvent reorganization energy λ were assumed to be 40 and 35 cm^{-1}, respectively. To calculate the rate constants we used modified Förster/Redfield theory[26,27]. The rate constants are fully determined by the spectral density defined above and the electronic coupling constants. Here, the cutoff frequency dividing Förster and Redfield regimes was assumed to be 30 cm^{-1} so that if a given pair of pigments were coupled to each other weakly (less than 30 cm^{-1}) the excitation transfer process was treated as a Förster process. Denoting the exciton transport rate constant from the jth one-exciton state to the ith one-exciton state by k_{ij}, we found that $k_{21} = 0.12$, $k_{21} = 2.97$, $k_{13} = 0.12$, $k_{23} = 0.28$, $k_{24} = 5.38$, $k_{25} = 1.6$, $k_{26} = 0.22$, $k_{35} = 0.17$, $k_{37} = 1.6$, $k_{42} = 0.48$, $k_{45} = 2.0$, $k_{46} = 2.46$, $k_{54} = 0.91$, $k_{56} = 5.73$, $k_{57} = 0.16$, $k_{64} = 0.18$, $k_{65} = 0.92$, $k_{67} = 0.68$ and $k_{76} = 0.22$ (all in ps^{-1}). All other rate constants are smaller than 0.1 ps^{-1}. The initial populations of the seven exciton states were determined by using the experimental laser spectrum (Fig. 1d, red).

Received 29 November 2004; accepted 4 February 2005; doi:10.1038/nature03429.

1. Zewail, A. H. *Femtochemistry* (World Scientific, Singapore, 1994).
2. Asplund, M. C., Zanni, M. T. & Hochstrasser, R. M. Two-dimensional infrared spectroscopy of peptides by phase-controlled femtosecond vibrational photon echoes. *Proc. Natl Acad. Sci. USA* **97,** 8219–8224 (2000).
3. Mukamel, S. Multidimensional femtosecond correlation spectroscopies of electronic and vibrational excitations. *Annu. Rev. Phys. Chem.* **51,** 691–729 (2000).
4. Wright, J. C. Coherent multidimensional vibrational spectroscopy. *Int. Rev. Phys. Chem.* **21,** 185–255 (2002).
5. Khalil, M., Demirdöven, N. & Tokmakoff, A. Coherent 2D IR spectroscopy: Molecular structure and dynamics in solution. *J. Phys. Chem. A* **107,** 5258–5279 (2003).
6. Asbury, J. B. *et al.* Hydrogen bond dynamics probed with ultrafast infrared heterodyne-detected multidimensional vibrational stimulated echoes. *Phys. Rev. Lett.* **91,** 237402 (2003).
7. Cervetto, V., Helbing, J., Bredenbeck, J. & Hamm, P. Double-resonance versus pulsed Fourier transform two-dimensional infrared spectroscopy: An experimental and theoretical comparison. *J. Chem. Phys.* **121,** 5935–5942 (2004).
8. Jonas, D. M. Two-dimensional femtosecond spectroscopy. *Annu. Rev. Phys. Chem.* **54,** 425–463 (2003).
9. Fenna, R. E. & Matthews, B. W. Chlorophyll arrangement in a bacteriochlorophyll protein from *Chlorobium limicola*. *Nature* **258,** 573–577 (1975).
10. Li, Y.-F., Zhou, W., Blankenship, R. E. & Allen, J. P. Crystal structure of the bacteriochlorophyll *a* protein from *Chlorobium tepidum*. *J. Mol. Biol.* **271,** 456–471 (1997).
11. Blankenship, R. E. *Molecular Mechanisms of Photosynthesis* (Blackwell, Oxford, 2002).
12. Blankenship, R. E. & Matsuura, K. in *Light-Harvesting Antennas in Photosynthesis* (eds Green, B. R. & Parson, W. W.) 195–217 (Kluwer Academic, Dordrecht, 2003).
13. Savikhin, S., Buck, D. R. & Struve, W. S. Toward level-to-level energy transfers in photosynthesis: The Fenna–Matthews–Olson protein. *J. Phys. Chem. B* **102,** 5556–5565 (1998).
14. Vulto, S. I. E. *et al.* Exciton simulations of optical spectra of the FMO complex from the green sulfur bacterium *Chlorobium tepidum* at 6 K. *J. Phys. Chem. B* **102,** 9577–9582 (1998).
15. Vulto, S. I. E. *et al.* Excited state dynamics in FMO antenna complexes from photosynthetic green sulfur bacteria: A kinetic model. *J. Phys. Chem. B* **103,** 8153–8161 (1999).
16. Wendling, M. *et al.* The quantitative relationship between structure and polarized spectroscopy in the FMO complex of *Prosthecochloris aestuarii*: Refining experiments and simulations. *Photosynth. Res.* **71,** 99–123 (2002).
17. Lepetit, L. & Joffre, M. Two-dimensional nonlinear optics using Fourier-transform spectral interferometry. *Opt. Lett.* **21,** 564–566 (1996).
18. Tian, P., Keusters, D., Suzaki, Y. & Warren, W. S. Femtosecond phase-coherent two-dimensional spectroscopy. *Science* **300,** 1553–1555 (2003).
19. Cowan, M. L., Ogilvie, J. P. & Miller, R. J. D. Two-dimensional spectroscopy using diffractive optics based phased-locked photon echoes. *Chem. Phys. Lett.* **386,** 184–189 (2004).
20. Brixner, T., Stopkin, I. V. & Fleming, G. R. Tunable two-dimensional femtosecond spectroscopy. *Opt. Lett.* **29,** 884–886 (2004).
21. Brixner, T., Mancal, T., Stopkin, I. V. & Fleming, G. R. Phase-stabilized two-dimensional electronic spectroscopy. *J. Chem. Phys.* **121,** 4221–4236 (2004).
22. Cho, M. Nonlinear response functions for three-dimensional spectroscopies. *J. Chem. Phys.* **115,** 4424–4437 (2001).
23. Prall, B. S., Parkinson, D. Y., Fleming, G. R., Yang, M. & Ishikawa, N. Two-dimensional optical spectroscopy: Two-color photon echoes of electronically coupled phthalocyanine dimers. *J. Chem. Phys.* **120,** 2537–2540 (2004).
24. Tokmakoff, A. Two-dimensional line shapes derived from coherent third-order nonlinear spectroscopy. *J. Phys. Chem. A* **104,** 4247–4255 (2000).
25. Kwac, K. & Cho, M. Two-color pump-probe spectroscopies of two- and three-level systems: Two-dimensional line shapes and solvation dynamics. *J. Phys. Chem. A* **107,** 5903–5912 (2003).
26. Zhang, W. M., Meier, T., Chernyak, V. & Mukamel, S. Exciton-migration and three-pulse femtosecond optical spectroscopies of photosynthetic antenna complexes. *J. Chem. Phys.* **108,** 7763–7774 (1998).
27. Yang, M., Damjanovic, A., Vaswani, H. M. & Fleming, G. R. Energy transfer in photosystem I of cyanobacteria *Synechococcus elongatus*: Model study with structure-based semi-empirical Hamiltonian and experimental spectral density. *Biophys. J.* **85,** 140–158 (2003).
28. van Amerongen, H., Valkunas, L. & van Grondelle, R. *Photosynthetic Excitons* (World Scientific, Singapore, 2000).
29. Maznev, A. A., Nelson, K. A. & Rogers, T. A. Optical heterodyne detection of laser-induced gratings. *Opt. Lett.* **23,** 1319–1321 (1998).
30. Goodno, G. D., Dadusc, G. & Miller, R. J. D. Ultrafast heterodyne-detected transient-grating spectroscopy using diffractive optics. *J. Opt. Soc. Am. B* **15,** 1791–1794 (1998).

Acknowledgements We thank Y.-Z. Ma, L. Valkunas and M. Yang for discussions, and C. Goodhope for protein purification. The apparatus for 2D spectroscopy was constructed by I. V. Stiopkin and T.B. This work was supported by the DOE (at LBNL, UC Berkeley and Arizona State University), and by a CRIP grant to M.C. by KOSEF (Korea). T.B. thanks the German Science Foundation (DFG) for an Emmy Noether fellowship, and J.S. thanks the German Academic Exchange Service (DAAD) for a postdoctoral fellowship.

Competing interests statement The authors declare that they have no competing financial interests.

Correspondence and requests for materials should be addressed to G.R.F. (grfleming@lbl.gov) and M.C. (mcho@korea.ac.kr).

Decline of the marine ecosystem caused by a reduction in the Atlantic overturning circulation

Andreas Schmittner

College of Oceanic and Atmospheric Sciences, Oregon State University, 104 COAS Admin. Bldg, Corvallis, Oregon 97331, USA

Reorganizations of the Atlantic meridional overturning circulation were associated with large and abrupt climatic changes in the North Atlantic region during the last glacial period[1–4]. Projections with climate models suggest that similar reorganizations may also occur in response to anthropogenic global warming[5–7]. Here I use ensemble simulations with a coupled climate–ecosytem model of intermediate complexity to investigate the possible consequences of such disturbances to the marine ecosystem. In the simulations, a disruption of the Atlantic meridional overturning circulation leads to a collapse of the North Atlantic plankton stocks to less than half of their initial biomass, owing to rapid shoaling of winter mixed layers and their associated separation from the deep ocean nutrient reservoir. Globally integrated export production declines by more than 20 per cent owing to reduced upwelling of nutrient-rich deep water and gradual depletion of upper ocean nutrient concentrations. These model results are consistent with the available high-resolution palaeorecord, and suggest that global ocean productivity is sensitive to changes in the Atlantic meridional overturning circulation.

The climatic consequences of Atlantic meridional overturning (AMO) reorganizations have been intensely documented in recent decades[1–4]. Temperature oscillations in Greenland, recorded in the isotopic composition of the ice, show rapid warmings of about 10 °C, known as Dansgaard–Oeschger events, coincident with abrupt increases of sea surface temperature (SST) and sea surface salinity (SSS) in the North Atlantic. During the cold (stadial) phases of the oscillations, deep water formation in the North Atlantic was partially or entirely stopped[3], leading to reduced northward heat transport by the ocean. Observed spatial patterns, amplitudes and phasing of temperature changes associated with Dansgaard–Oeschger oscillations can be successfully reproduced with coupled climate models forced with disturbances of the Atlantic freshwater budget[4]. However, the consequences of AMO changes for the marine ecosystem have not yet been quantified on a global scale. This will be particularly important, as projections of future climate change indicate that the AMO could weaken or even disappear in the coming centuries owing to anthropogenic greenhouse gas emissions[5–7]. Here I examine the impact of changes in ocean circulation on the marine ecosystem.

A climate model of intermediate complexity is used, including

four different formulations of simple upper ocean ecosystem components (see Methods section for a more detailed description and references). In order to trigger transitions between different states of the AMO, a slowly varying freshwater perturbation to the North Atlantic (Fig. 1a) is applied, following ref. 4. This leads to a gradual spindown of the circulation from about 16 Sv at year 0 to less than 3 Sv at year 500. Associated with this spindown is a reduction of convection and deep water formation and strong cooling (not shown here; see, for example, ref. 4) in the North Atlantic. This represents the transition from an interstadial (warm) to a stadial (cold) phase of the Dansgaard–Oeschger oscillations. The climate system remains in the stadial mode for more than 800 yr until around year 1,340 when a rapid return to interstadial conditions occurs.

After the AMO spindown, global export production (through the sinking of particulate organic matter), as well as primary production and biomass, slowly decrease by up to 10–20% around year 1,200 (Fig. 1b–d). The decrease in productivity is caused by a reduction of the upper ocean nutrient concentrations (Fig. 1e). Export production in the Atlantic rapidly reduces by 40% until year 500 (Fig. 1f). In the Indian and Pacific oceans, productivity decline is slower and reaches one-third around years 1,000 and 1,200, respectively. In the Southern Ocean, relative changes are smaller (10%) than in the other basins.

The response is most dramatic in the North Atlantic. Integrated plankton stocks north of 35° N plunge by 51 ± 8% from year 0 to year 500 (Fig. 1g). Annual net primary productivity in most of the North Atlantic collapses (Fig. 2d). Nutrient concentrations in today's North Atlantic are relatively small (Fig. 3a, c). However, winter mixed layers are deep, allowing replenishment of surface nutrient levels from quite large depths. Shoaling of mixed layers (Figs 1i, 3e) as a consequence of the AMO reduction and the associated development of a strong halocline decreases nutrient supply to the photic zone, leading to rapid plankton demise.

After deep water formation has ceased, nutrient levels slowly increase in the North Atlantic (Fig. 1h) owing to horizontal advection and diffusion along isopycnals, and a shallow nutricline develops (Fig. 3e), similar to the present situation in the North Pacific (Fig. 3b, d). This is in good agreement with glacial reconstructions suggesting higher nutrient levels in the deep and intermediate North Atlantic during cold phases[2,8]. (Note that carbon isotope ratios used as nutrient proxies in refs 2 and 8 might also be influenced by air–sea gas exchange.) In the top 1 km of the Pacific, Indian and South Atlantic oceans, nutrient levels decrease while deep sea nutrient concentrations increase owing to missing injection of low-nutrient North Atlantic Deep Water (Fig. 3). Deep upwelling in the Indo-Pacific is reduced by 50% (4 Sv), contributing directly to lesser nutrients there. Upwelling across 1,000 m into the Southern Ocean (south of 35° S) diminishes by 10 Sv, causing lower nutrient concentrations in the formation areas of Subantarctic Mode Water (SAMW). Large regions of the world's upper oceans are currently supplied with nutrients by SAMW[9]. Thus, lower nutrient levels of SAMW reduce nutrient supply to these regions, as analysis of the individual term balances of the upper ocean

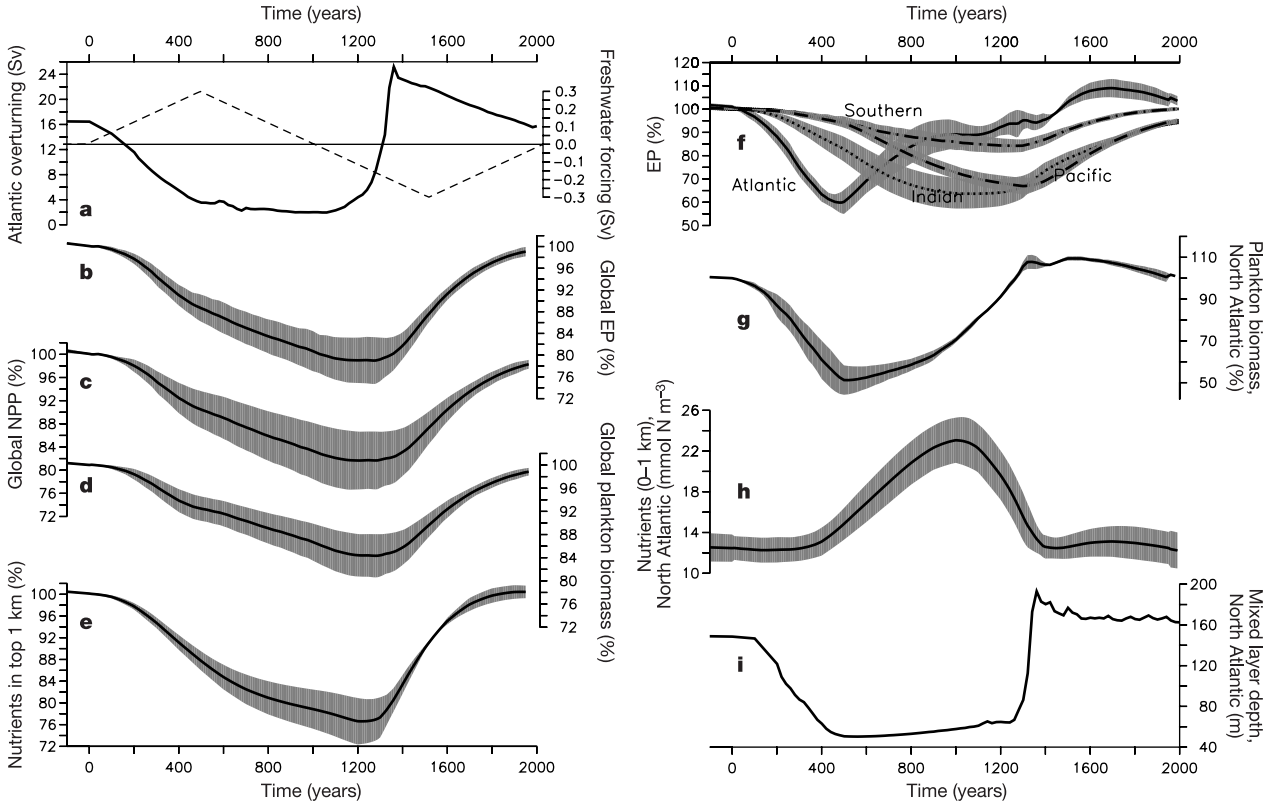

Figure 1 Time series from the model simulations. Left panels show freshwater forcing in the North Atlantic (dashed line, right scale) and AMO circulation (solid line, left scale) (**a**), globally integrated export production, EP (**b**), net primary production, NPP (**c**), plankton (phytoplankton plus zooplankton) stocks (**d**) and nutrient concentrations in the top 1 km (**e**). Right panels show changes in integrated export production (**f**) in the individual ocean basins (Atlantic, solid; Pacific, dashed; Indian, dotted; Southern Ocean, dash-dotted) as well as integrated biomass (**g**), average nitrate concentrations (**h**) and average mixed layer depth (calculated as depth of $\Delta\sigma_\theta = 0.25$ using annual mean densities) in the North Atlantic from 35° N to 70° N (**i**; rectangle in Fig. 2). Panels **b**–**g** give percentage changes with respect to year 0. The grey bars enclosing the ensemble mean (solid lines) denote the standard deviation of the different ecosystem models used and represent the uncertainties associated with the formulation and parameterizations of the ecosystem models. The evolution of the physical variables does not vary between the different experiments, hence panels **a** and **i** do not contain shadings.

nutrient budget confirmed (not shown). In the North Atlantic, increasing subsurface nutrient levels lead to a gradual recovery of plankton stocks after year 500 (Fig. 1g). Around year 1,200, that is, 700 yr after the collapse, North Atlantic plankton stocks re-attain their initial size. Note that this occurs before the resumption of the circulation around year 1,340.

The simulated evolution of productivity in the North Atlantic (Fig. 4a) is consistent with recent reconstructions[10–12]. A qualitative productivity record of high temporal resolution from the Reykjanes ridge (60° N, 30° W), based on planktonic and benthic foraminifera species composition and accumulation rates, indicates low productivity during stadials and high productivity during interstadials[11]. This is in agreement with the simulations, which show stadial productivity reduced by about 40%. Consistently, a record of benthic species composition from the northeast Atlantic (50° N, 20° W) also indicates low productivity during Heinrich events[12]. A quantitative reconstruction of productivity from the northeast Atlantic[10] (53° N, 19° W) shows about 50% decrease during cold and fresh episodes with respect to warm and saline periods, consistent with the simulations.

A fast reduction of productivity and planktonic biomass is also simulated in the equatorial and South Atlantic (Figs 2d, 4a). In the western equatorial Atlantic (61° W, 12° N), productivity decreases by 25–50%, consistent with a high-resolution record of dinoflagellate cyst and organic carbon accumulation at this site. The reduced productivity during the stadial Dansgaard–Oeschger phases[13] has been attributed to variations in the Orinoco River nutrient discharge and coastal upwelling strength. These processes are not included in the simulation, which shows a decrease in response to thermohaline driven changes in ocean circulation only. In the eastern South Atlantic, productivity drops dramatically during the first 500 yr of the simulations and remains low throughout the stadial. Reversal of the upper ocean flow direction (Fig. 3c, e) from mainly northward at year 0 to southward after year 500 cuts off the South Atlantic from a supply of high-nutrient waters of southern origin. Additionally, reduced upwelling decreases nutrients in the southeast Atlantic.

Productivity also declines in the Arabian Sea and the eastern tropical Indian Ocean, as well as in the Southern Ocean. In the Arabian Sea at 66° E, 23° N, for example, productivity decreases by about 40% until year 1,200 (Fig. 4b). This is consistent with recent alkenone-based reconstructions from this site[14] suggesting higher productivity during interstadials and lower productivity during stadials. However, in the simulation this is caused by purely thermohaline-driven changes in upwelling and not through wind-driven upwelling as suggested previously[14].

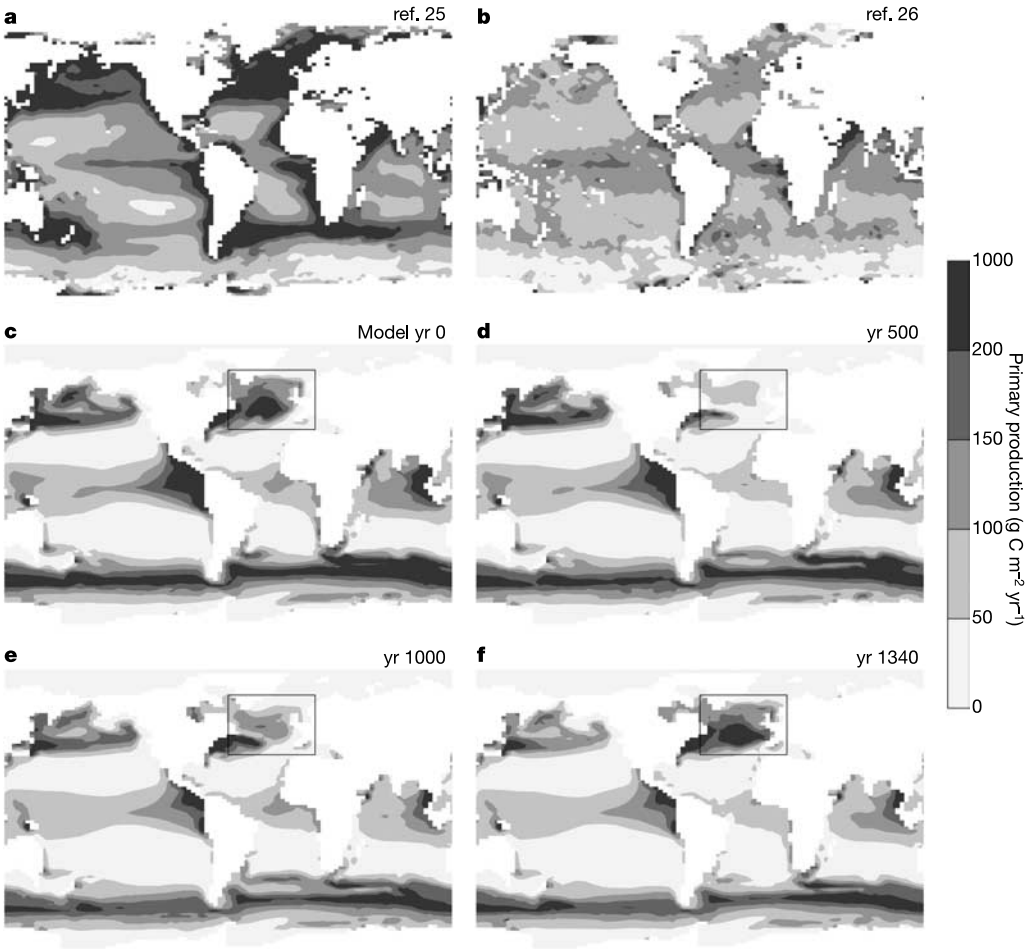

Figure 2 Annual net primary productivity from observations and the ensemble mean of the simulations. Differences between the two estimates based on satellite observations[25,26] (**a**, **b**) represent mainly uncertainties associated with algorithms used to infer vertically integrated productivity from ocean colour (chlorophyll) observations. The ensemble mean during the initial state of an operating AMO at year 0 (**c**) is compared with the satellite estimates in the Methods section. Snapshots during the simulations show the collapsed AMO at year 500 at minimum productivity in the North Atlantic (**d**), the state at year 1,000 during minimum global productivity (**e**) and the situation during the rapid recovery at year 1,340 (**f**). The squares denote the area in the North Atlantic for which averaged time series are shown in Fig. 1.

After entering the stadial state at year 500, the ecosystem also declines in the North Pacific, the eastern tropical Pacific and in the Southern Ocean owing to gradual depletion of surface nutrients there (Figs 3, 4). High-resolution records from the northeast Pacific demonstrate anoxic conditions during interstadials and better oxygenation during stadials[15,16]. This has been explained by changes in intermediate water mass ventilation[15] and/or surface water productivity[16]. In the simulation, productivity at 120° W, 34° N decreases by up to 50% from interstadial to stadial levels. Lower productivity leads to slower rates of remineralization of organic matter, and therefore to reduced consumption of oxygen at depth. Thus, the simulation is consistent with the record, and supports the hypothesis that reduced productivity was at least partly responsible for the higher oxygen concentrations during the cold events. However, contrary to speculations that changes in ENSO (El Niño/Southern Oscillation) were responsible for the stadial productivity minimum[16], in the simulation it is solely caused by thermohaline-driven reduction in upwelling.

The AMO spindown does not decrease productivity everywhere. Along the eastern boundary current of the North Atlantic subtropical gyre, for example, productivity increases during the first 750 yr of the simulation (Figs 2, 4). At 20° W, 26° N (the location of sediment core 15637) and at 20° W, 40° N (along the Iberian margin), productivity increases by up to a factor of five during the stadial. Palaeoproductivity records from these sites[17,18] indicate increased productivity by a factor of two or more during cold events, consistent with the model results. Analysis of the simulation indicates that increasing subsurface nutrient concentrations and stronger upwelling fertilize the ocean along the Iberian and North African coasts during the stadials.

Taken together (Fig. 4), the available proxy record corroborates the model results. However, a more stringent and quantitative test is at present hampered by the low temporal and spatial resolution of existing productivity records. Particularly desirable would be additional records from the South(east) Atlantic, the Southern Ocean and from the tropical, south and northwest Pacific.

This Letter has examined the influence of circulation changes on the marine ecosystem. In the case of enhanced future global

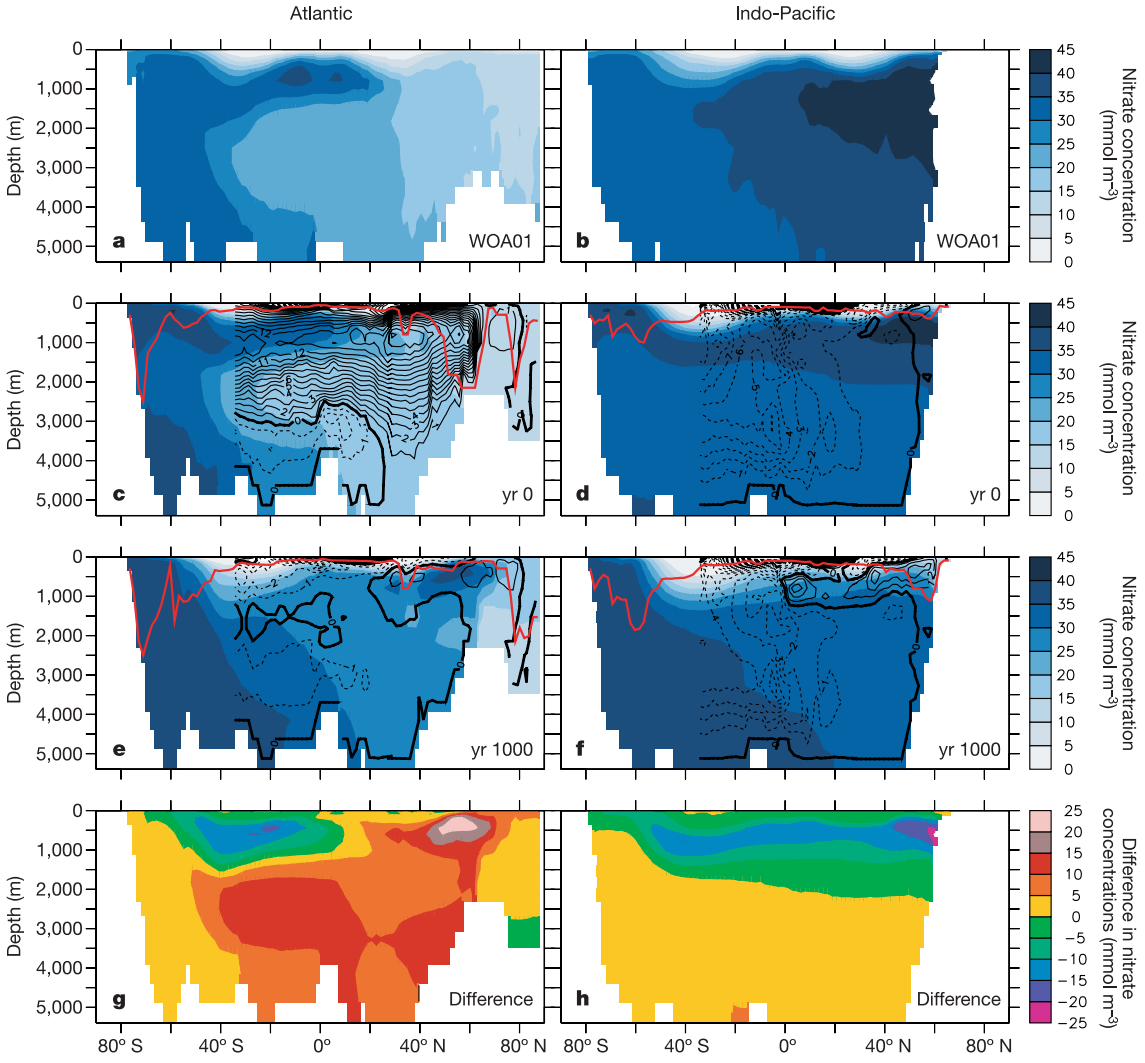

Figure 3 Latitude-depth sections of zonally averaged nitrate concentrations in mmol m^{-3}. Modern observations[28] (**a**, **b**) and model results from year 0 (**c**, **d**), at year 1,000 (**e**, **f**) and the difference between year 1,000 and year 0 (**g**, **h**) in the Atlantic (left) and Indo-Pacific (right). Black contour lines give the zonally integrated eulerian circulation in sverdrups (1 Sv = 10^6 m^3 s^{-1}), and red lines denote the zonal and annual maximum monthly mixed layer depth (calculated as depth of $\Delta\sigma_\theta = 0.1$ kg m^{-3}). In the case of an active overturning (**a**, **c**), the North Atlantic is nutrient depleted owing to extraction of nutrients along the northward path of the upper branch of the circulation. Low-nutrient North Atlantic Deep Water (NADW) then flows southward at around 2,000 m depth. After the AMO stops, nutrient levels increase in the North Atlantic (**e**, **g**) and a subsurface nutrient maximum develops much like in today's North Pacific (**b**, **d**), while concentrations decrease in the top 1 km of the South Atlantic, Southern and Indo-Pacific oceans (**e**–**h**).

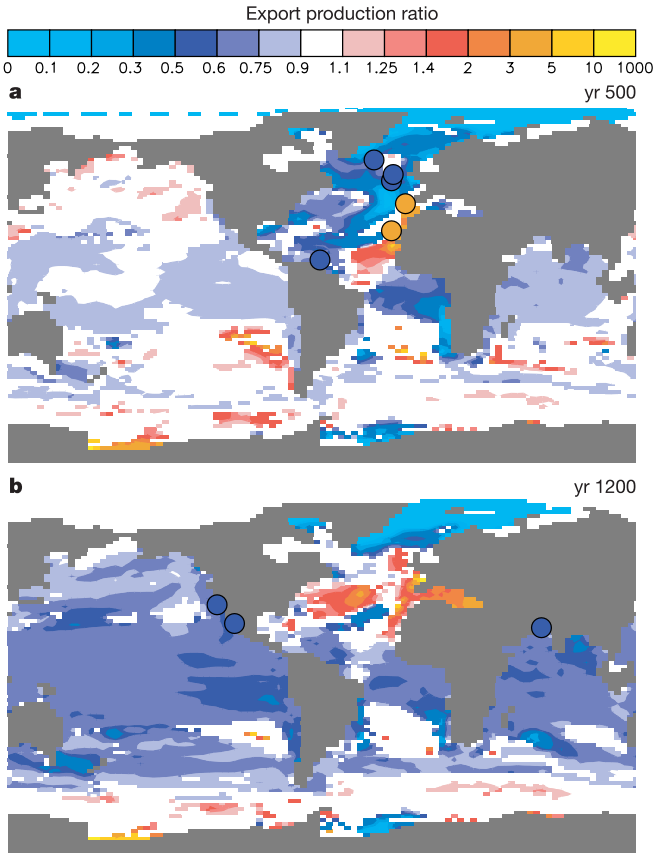

Figure 4 Comparison of simulated changes in export production with palaeoproductivity proxy records. Coloured circles show the proxy records. Colour contours give the model ensemble mean ratio of export production during the early stadial stage (**a**; yr 500) and the late stadial stage (**b**; yr 1,200) with respect to interstadial (model year 0) values. A value of 0.3, for example, indicates export production decreased by 70%. Only statistically significant values are plotted, in the sense that the mean ± the standard deviation is not allowed to include one (no change). Blue coloured circles denote lower productivity during stadials, and orange coloured circles denote increased productivity as inferred from the proxy records discussed in the main text. Note that only qualitative changes are shown for the palaeorecords, as most reconstructions give no quantitative estimates. As the largest productivity changes are simulated in the North Atlantic during the early stadial stage (see Fig. 1) while in the Indian and Pacific oceans the largest changes occur during the late stadial stage, the Atlantic proxy records are shown in the upper panel[10–13,17,18] and the Indian and Pacific records in the lower panel[14–16].

warming, additional effects such as increased stratification due to upper ocean warming will affect marine productivity[19]. Moreover, in the simulations presented above, the AMO spindown is relatively slow (about 500 yr, see Fig. 1). More rapid reductions as projected by some models[5–7] would presumably lead to an even stronger decline in biomass, particularly in the North Atlantic. From Fig. 1 it appears that even a partial weakening of the overturning causes a substantial reduction of productivity. The results presented above have important implications for the assessment of future greenhouse gas emission scenarios. A massive decline of plankton stocks could have catastrophic effects on fisheries and human food supply in the affected regions. Hence, emission pathways that lead to fast and large increases of future CO_2 including the risk of a collapse or substantial reduction of the AMO[6] should be avoided through early measures for emission reductions. □

Methods

Climate model

For the simulations presented in this Letter, I use the University of Victoria Earth System Climate Model[20]. This is a global model consisting of a fully nonlinear primitive equations three-dimensional ocean circulation model using a scheme of tidal mixing[21] (which leads to low values of vertical diffusion of 0.2–0.3 $cm^2 s^{-1}$ within the pycnocline), a dynamic thermodynamic state-of-the-art sea ice component and a single level energy moisture balance model of the atmosphere. A prescribed seasonal cycle of present-day near surface atmospheric wind velocities is used in the advection of specific humidity, for the momentum transfer to the surface ocean and sea ice and in the calculation of surface sensible and latent heat fluxes. As such, the atmospheric hydrological cycle is interactive and considers thermodynamic effects (Clausius–Clapeyron) but neglects dynamic effects (for example, changes in the Hadley circulation). The model response might therefore be different from a model with a more complete, dynamical atmospheric component. The simulations presented above use a preindustrial (interglacial) background climate (for example, present-day sea level, atmospheric CO_2 concentration of 280 p.p.m.v.). However, an equivalent simulation under glacial conditions confirmed the results presented.

Ecosystem models and simulations

The models of the marine ecosystem dynamics, solving prognostic equations for nutrients, phytoplankton, zooplankton, detritus and dissolved organic matter, based on nitrate as the limiting nutrient, have been interactively coupled to the ocean circulation component of the model[22]. In order to consider uncertainties in the formulation of the ecosystem models, identical (ensemble) simulations have been performed with four different models. The four ensemble members represent two versions from ref. 22 (termed 'REF' and 'tidal $K_b = 0.2$, $\sigma_{DOM} = 0.15$ $\mu_{DOM} = 0.17$' in Table 1 of ref. 22), the formulation of ref. 23 and the model of ref. 24. The difference between the first two is the inclusion of dissolved organic matter cycling, and the last two models use fundamentally different formulations and parameterizations. All four models produce similarly good agreement with global nutrient (Fig. 3) and chlorophyll (phytoplankton) observations. The model of ref. 24 uses a parameterization of fast microbial nutrient recycling through ammonium which increases productivity mainly at low latitudes. This leads to global primary productivity of 48.6 Gt C yr^{-1}, which is in better agreement with observations (36–50 Gt C yr^{-1})[25,26] than the values of 20–30 Gt C yr^{-1} of the other models. The ensemble mean primary productivity for modern conditions (Fig. 2c) is broadly consistent with satellite estimates within their uncertainties (Fig. 2a, b). Areas of high productivity are the mid-latitudes of the Northern Hemisphere, the equatorial upwelling areas, the Southern Ocean and the zonal boundary currents.

Systematic biases occur in the centres of the subtropical gyres, where most models are too oligotrophic. The Southern Ocean is too eutrophic in most models, and the belt of maximum productivity is located too far south. Despite the large differences between the individual models, certain aspects (such as nitrogen fixation and denitrification, as well as limitation by nutrients other than nitrate) are not taken into account in either model. It is therefore possible, that for example, the neglect of iron limitation biases the results in iron-limited regions. But because the vertical profile of iron in the ocean is similar to that of the other nutrients (low values in the euphotic zone and high concentrations at depths), and because it has been estimated that only 25% of the iron supply to the phytoplankton comes from atmospheric deposition whereas 75% is supplied through upwelling[27], it can be assumed that reduced upwelling also leads to a reduced iron supply. This suggests that missing iron limitation does not qualitatively affect the results. Generally, the reliability of the results presented above will be better in nitrate-limited regions, such as the North Atlantic, and probably less in regions that are thought to be limited by other nutrients (like the iron-limited Southern Ocean and the equatorial Pacific). Note also that the sensitivity of the AMO to perturbations might be strongly model dependent, as indicated by the large scatter in future projections[7].

Received 6 August 2004; accepted 7 February 2005; doi:10.1038/nature03476.

1. Clark, P. U., Pisias, N. G., Stocker, T. F. & Weaver, A. J. The role of the thermohaline circulation in abrupt climate change. *Nature* **415,** 863–869 (2002).
2. Sarnthein, M. *et al.* in *The Northern North Atlantic: A Changing Environment* (eds Schäfer, P., Ritzau, W., Schlüter, M. & Thiede, J.) 45–66 (Springer, Berlin, 2001).
3. Dokken, T. M. & Jansen, E. Rapid changes in the mechanism of ocean convection during the last glacial period. *Nature* **401,** 458–461 (1999).
4. Schmittner, A., Saenko, O. A. & Weaver, A. J. Coupling of the hemispheres in observations and simulations of glacial climate change. *Quat. Sci. Rev.* **22,** 659–671 (2003).
5. Manabe, S. & Stouffer, R. J. Century-scale effects of increased atmospheric CO_2 on the ocean-atmosphere system. *Nature* **364,** 215–218 (1993).
6. Stocker, T. F. & Schmittner, A. Influence of CO_2 emission rates on the stability of the thermohaline circulation. *Nature* **388,** 862–865 (1997).
7. Cubasch, U. *et al.* in *Climate Change 2001: The Scientific Basis* (ed. Houghton, J. T.) 525–582 (Cambridge Univ. Press, Cambridge, 2001).
8. Willamowski, C. & Zahn, R. Upper ocean circulation in the glacial North Atlantic from benthic foraminiferal isotope and trace element fingerprinting. *Paleoceanography* **15,** 515–527 (2000).
9. Sarmiento, J. L., Gruber, N., Brzezinski, M. A. & Dunne, J. P. High-latitude controls of thermocline nutrients and low latitude biological productivity. *Nature* **427,** 56–60 (2003).
10. Weinelt, M., Rosell-Mele, A., Pflaumann, U., Sarnthein, M. & Kiefer, T. Zur Rolle der Produktivität im Nordostatlantik bei abrupten Klimaänderungen in den letzten 80000 Jahren. *Z. Dt. Geol. Ges.* **154,** 47–66 (2003).
11. Rasmussen, T. L., Thomson, E., Troelstra, S. R., Kuijpers, A. & Prins, M. A. Millennial-scale glacial variability versus Holocene stability: changes in planktic and benthic foraminiferal faunas and ocean circulation in the North Atlantic during the last 60 000 years. *Mar. Micropaleont.* **47,** 143–176 (2002).
12. Thomas, E., Booth, L., Maslin, M. & Shackleton, N. J. Northeastern Atlantic benthic foraminifera during the last 45,000 years: Changes in productivity seen from the bottom up. *Paleoceanography* **10,** 545–562 (1995).
13. Vink, A. *et al.* Shifts in the position of the North Equatorial Current and rapid productivity changes in the western Tropical Atlantic during the last glacial. *Paleoceanography* **16,** 479–490 (2001).

14. Schulte, S. & Müller, P. J. Variations of sea surface temperature and primary productivity during Heinrich and Dansgaard-Oeschger events in the northeastern Arabian Sea. *Geo-Mar. Lett.* **21,** 168–175 (2001).
15. Hendy, I. L. & Kennett, J. P. Tropical forcing of North Pacific intermediate water distribution during Late Quaternary rapid climate change? *Quat. Sci. Rev.* **22,** 673–689 (2003).
16. Ortiz, J. D. *et al.* Enhanced productivity off western North America during the warm climate intervals of the past 52 k.y. *Geology* **32,** 521–524 (2004).
17. Kiefer, T. *Productivity and Temperatures in the Subtropical North Atlantic: Cyclic and Abrupt Changes During the Late Quaternary* (Rep. No. 90, Geol.-Paläont. Inst. Univ. Kiel, 1998).
18. Lebreiro, S. M., Moreno, J. C., Abrantes, F. F. & Pflaumann, U. Productivity and paleoceanographic implications on the Tore Seamount (Iberian Margin) during the last 225 kyr: Foraminiferal evidence. *Paleoceanography* **12,** 718–727 (1997).
19. Bopp, L. *et al.* Potential impact of climate change on marine export production. *Glob. Biogeochem. Cycles* **15,** 81–100 (2001).
20. Weaver, A. J. *et al.* The UVic Earth system climate model: Model description, climatology and applications to past, present and future climates. *Atmosphere-Ocean* **4,** 361–428 (2001).
21. Simmons, H. L., Jayne, S. R., St Laurent, L. C. & Weaver, A. J. Tidally driven mixing in a numerical model of the ocean general circulation. *Ocean Model.* **6,** 245–263 (2004).
22. Schmittner, A., Oschlies, A., Giraud, X., Eby, M. & Simmons, H. L. A global model of the marine ecosystem for long term simulations: sensitivity to ocean mixing, buoyancy forcing, particle sinking and dissolved organic matter cycling. *Glob. Biogeochem. Cycles* (in the press).
23. Six, K. D. & Maier-Reimer, E. Effects of plankton dynamics on seasonal carbon fluxes in an ocean general circulation model. *Glob. Biogeochem. Cycles* **10,** 559–583 (1996).
24. Schartau, M. & Oschlies, A. Simultaneous data-based optimization of a 1D-ecosystem model at three locations in the North Atlantic: Part I–Method and parameter estimates. *J. Mar. Res.* **61,** 765–793 (2003).
25. Gregg, W. W., Conkright, M. E., Ginoux, P., O'Reilly, J. E. & Casey, N. W. Ocean primary production and climate: Global decadal changes. *Geophys. Res. Lett.* **30,** 1809, doi:10.1029/2003GL016889 (2003).
26. Antoine, D., André, J.-M. & Morel, A. Oceanic primary production 2. Estimation at global scale from satellite (coastal zone color scanner) chlorophyll. *Glob. Biogeochem. Cycles* **10,** 57–69 (1996).
27. Aumont, O., Maier-Reimer, E., Blain, S. & Monfray, P. An ecosystem model of the global ocean including Fe, Si, P colimitations. *Glob. Biogeochem. Cycles* **17,** 1060, doi:10.1029/2001GB001745 (2003).
28. Conkright, M. E. *et al. World Ocean Atlas 2001, Objective Analysis, Data Statistics, and Figures* (CD-ROM Documentation, National Oceanographic Data Center, Silver Spring, Maryland, 2002).

Acknowledgements Productivity data sets were provided by D. Antoine and W. Gregg. Discussions with A. Oschlies, M. Sarnthein, M. Weinelt and H. Kinkel were appreciated. This research was supported as part of the research unit (Forschergruppe 451) on ocean gateways by the Deutsche Forschungsgemeinschaft (DFG).

Competing interests statement The authors declare that they have no competing financial interests.

Correspondence and requests for materials should be addressed to A.S. (aschmittner@coas.oregonstate.edu).

Structural and temporal requirements for geomagnetic field reversal deduced from lava flows

Brad S. Singer[1], Kenneth A. Hoffman[2], Robert S. Coe[3], Laurie L. Brown[4], Brian R. Jicha[1], Malcolm S. Pringle[5] & Annick Chauvin[6]

[1]*Department of Geology and Geophysics, University of Wisconsin, Madison, Wisconsin 53706, USA*
[2]*Physics Department, California Polytechnic State University, San Luis Obispo, California 93407, USA*
[3]*Earth Sciences Department, University of California, Santa Cruz, California 95064, USA*
[4]*Department of Geosciences, University of Massachusetts, Amherst, Massachusetts 01003, USA*
[5]*Department of Earth, Atmospheric, and Planetary Sciences, Massachusetts Institute of Technology, Cambridge, Massachusetts 02139, USA*
[6]*Geosciences Rennes UMR-CNRS, Campus Beaulieu, Bâtiment 15, 35042 Rennes Cedex, France*

Reversals of the Earth's magnetic field reflect changes in the geodynamo—flow within the outer core—that generates the field. Constraining core processes or mantle properties that induce or modulate reversals requires knowing the timing and morphology of field changes that precede and accompany these reversals[1–4]. But the short duration of transitional field states and fragmentary nature of even the best palaeomagnetic records make it difficult to provide a timeline for the reversal process[1,5]. $^{40}Ar/^{39}Ar$ dating of lavas on Tahiti, long thought to record the primary part of the most recent 'Matuyama–Brunhes' reversal, gives an age of 795 ± 7 kyr, indistinguishable from that of lavas in Chile and La Palma that record a transition in the Earth's magnetic field, but older than the accepted age for the reversal. Only the 'transitional' lavas on Maui and one from La Palma (dated at 776 ± 2 kyr), agree with the astronomical age for the reversal. Here we propose that the older lavas record the onset of a geodynamo process, which only on occasion would result in polarity change. This initial instability, associated with the first of two decreases in field intensity, began ~18 kyr before the actual polarity switch. These data support the claim[6] that complete reversals require a significant period for magnetic flux to escape from the solid inner core and sufficiently weaken its stabilizing effect[7].

Most reversal records come from quasi-continuously deposited sediments[1,8–9] and many indicate that reversals occur when field intensity has diminished (see, for example, refs 10, 11). Establishing the rate of sediment accumulation may reveal a duration for the reversal process, but accumulation rates are difficult to quantify[1]. One approach is to tune oxygen isotope variations orbitally down the section, estimate the astronomical ages of successive magnetic reversals[12] and interpolate the accumulation rate. With the use of

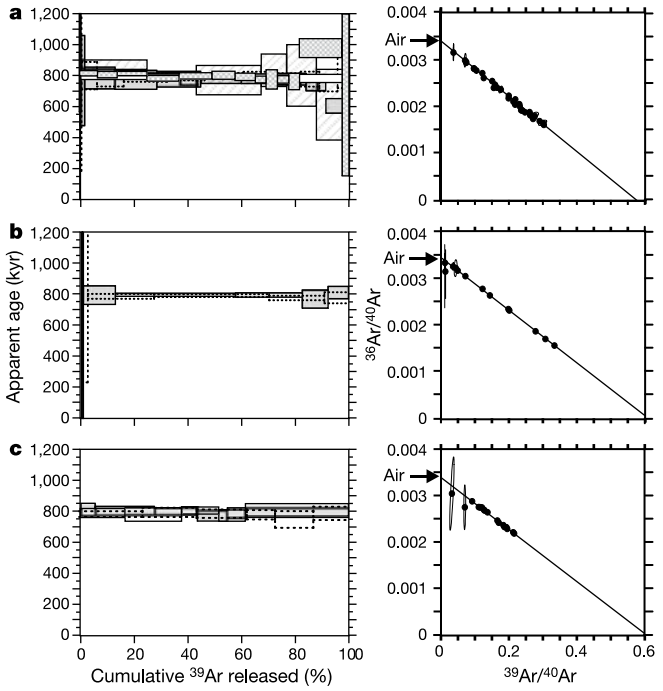

Figure 1 $^{40}Ar/^{39}Ar$ age spectra and isochrons from lavas TT, RIT and RIV in Punaruu Valley, Tahiti. The largely concordant spectra (left) and well-defined isochrons (right) indicate that extraneous argon is not a problem. Isochrons of several experiments on each lava were normalized to a common neutron fluence parameter J for illustrative purposes only. The weighted mean of the individual isochrons from several subsamples gives the best age (±2σ) for each lava. **a**, TT groundmass. The plateau is at 789.7 ± 5.2 kyr; the results are from five separate experiments. The isochron age is 798.0 ± 11.0 kyr, $^{40}Ar/^{36}Ar_i$ = 293.9 ± 3.6, MSWD = 0.15 and n = 32 of 39. **b**, R1V groundmass. The plateau is at 789.4 ± 6.5 kyr; the results are from two separate experiments. The isochron age is 791.9 ± 9.3 kyr, $^{40}Ar/^{36}Ar_i$ = 294.8 ± 1.9, MSWD = 0.04 and n = 13 of 13. **c**, R1T groundmass. The plateau is at 792.1 ± 7.6 kyr; the results are from three separate experiments. The isochron age is 798.0 ± 23.0 kyr, $^{40}Ar/^{36}Ar_i$ = 294.6 ± 2.9, MSWD = 0.70 and n = 18 of 18.